Does Selective Shell Printing Advance Binder Jetting Additive Manufacturing?

Meisam Khademitab [a], Mohammad Jamalkhani [a], Kejsi Bishaj [a], Ethan Jenssen [a,1], Mike Heim [b], Dave Nelson [b], Niall M. O'Dowd [c], Amir Mostafaei [a,*]

[a] Department of Mechanical, Materials, and Aerospace Engineering, Illinois Institute of Technology, 10 W 32nd Street, Chicago, IL 60616, USA
[b] Nel Pretech Corporation, 8420 183rd Place, Tinley Park, IL, 60487, USA
[c] Phase3D, 2415 W 19th Street, Chicago IL, 60608, USA
[1] An undergraduate student awarded by the Armour R&D program from the Dean's Office at Illinois Institute of Technology

* Corresponding author
Email addresses: mostafaei@iit.edu (A. Mostafaei)

Abstract

Study examines binder deposition methods (bulk vs. selective printing) and sintering atmospheres (vacuum vs. H_2) on binder jetted 316L stainless steel components. The density of the H_2-sintered specimens was found to be lower (up to 5%) compared to the vacuum-sintered parts with the final density of 99.7%. Grain size analysis indicated smaller grains in the H_2-sintered parts (~26 μm) compared to vacuum-sintered condition (~33 μm) in the bound area which could be attributed to the presence of residual pores that impeded grain growth. The H_2-sintered specimens exhibited an elongation of 25% and an ultimate tensile strength (UTS) of 460 MPa, whereas the vacuum-sintered parts displayed an elongation of 70% and a UTS of 550 MPa. Fractography analysis using microscopy and micro-computed tomography revealed ductile fracture in the vacuum-sintered samples, while the H_2-sintered parts exhibited a combination of brittle and ductile fracture due to remnant pores in the microstructure.

Keywords: Vacuum/hydrogen sintering atmosphere; Densification; Microstructure analysis; Mechanical properties; Micro-computed tomography; 316L stainless steel.

1. Introduction

Binder jetting is one of the advanced additive manufacturing (AM) processes to fabricate parts with a large variety of materials, complex shapes, and low cost [1]. In the process of binder jetting, the binder plays a pivotal role in shaping and defining the characteristics of green components. It comprises liquid polymer droplets that permeate the spaces between particles, facilitated by processes such as spreading and infiltration propelled by capillary pressure. The binder must satisfy precise criteria, encompassing chemical stability, appropriate rheological properties, effective affinity with powders, and ample binding strength [2,3]. In certain binder jet printers, such as M-Flex Innovent models (possible new models such as X1 160PRO™ after ExOne merged with Desktop Metal), a water- or solvent-based polymeric binder is gently heated (using a heating light passing over the powder bed at a temperature below 100 °C) before the

subsequent powder spreading step. This pre-heating step is employed to dehydrate the powder bed surface and reduce the likelihood of powder adhering to the roller's surface. During curing (at temperatures up to 185 °C which depend on chemistry of binder), polymer chains form pendular bonds between particles, contributing to the strength of the green parts [1]. Minimizing the amount of binder residue in binder jetted parts is crucial since it potentially leaves C, O, S, and N contamination at the particle surfaces, affecting densification behavior and subsequent properties of the densified components [4–6].

The binder jetting process consists of two main steps; First, the powder is deposited in the build box and rolled out the surface of powder using rollers to compact and smooth the powder bed surface. Second, jetting the polymeric liquid binder onto specific areas based on a computer-aided design model. During the binder jet printing, binder is jetted across the entire cross-section of each layer, following a 3D CAD model, to create an object. However, an alternative approach called shell or selective printing exists [7–9]. In shell printing, the binder is only jetted in the region near the surface to form a shell, while the core remains as loose powder. The shell with a certain thickness possesses sufficient strength to restrict movement of the loose powder in the core, allowing for depowdering and handling of the green part for sintering. Through the sintering process, the powder in both the shell and core consolidates, leading to the formation of a solid object [8,9]. Shell printing minimizes binder usage, speeds up debinding, and ensures compatibility with binder-sensitive materials.

The binder burnout or debinding process is a crucial step preceding densification at elevated temperatures [1,10]. Typically conducted before sintering or infiltration in the same furnace, it involves the pyrolysis of the polymer, eliminating its presence in the green part to facilitate pore removal. The temperature for binder burnout, determined through differential thermal analysis, is set in the range of 450 to 600 °C for 30-60 minutes, dependent on the binder's chemistry. This process involves heating the part to temperatures exceeding the polymer's decomposition temperature, encouraging the evaporation or decomposition of the polymeric species and leaving the green part with gaseous residues or newly formed gaseous constituents through reactions with adsorbed powder species or the flowing gas, including hydrogen.

The sintering atmosphere is a crucial post-printing step aimed at significantly increasing the relative density of the green part. By eliminating pores, the sintering process enhances the density from approximately 50% to over 98%. In the post-printing process, sintering is typically carried out under various conditions, including inert gas (such as N_2 and Ar), reducing atmosphere (such as H_2), or vacuum. Nitrogen absorption by metals can result in the formation of nitride, which affects mechanical properties. Additionally, Ar entrapment in pores can hinder the densification process during the final stages of sintering. While a reducing atmosphere like H_2 may be suitable for sintering active metals such as copper, the presence of trapped H_2O in the intermediate stage can impede the final sintering stage. Consequently, vacuum-sintering is preferred for binder jetted metals to promote densification, minimize gas-filled pore formation, prevent oxidation, and reduce

carbon contamination [11]. During the final stage of sintering process, pore healing occurs through the lattice diffusion of vacancies and the sintering rate decreases significantly [12,13]. Localized liquid formation at the sintering temperature accelerates densification, provided there are no entrapped air-filled porosities within the part. Vacuum-sintering initiates active evaporation-condensation during the initial stage and facilitates material removal from the convex to the concave surface of the pores during final densification. Although vacuum-sintering may lead to unwanted evaporation of alloying elements [14,15], it effectively eliminates excessive carbon, nitrogen, and oxygen introduced by the polymer binder in 3D printed materials [6,16]. The speed of the oxygen and carbon reaction to produce carbon monoxide (CO) at a specific temperature relies on factors such as the concentrations of oxygen and carbon in the solid material, the diffusivities of oxygen and carbon, the equilibrium pressure of the reaction product, and the surrounding ambient pressure. The equilibrium vapor pressure of CO over 316 L decreases with lower carbon and oxygen contents, making diffusion to the surface the rate-determining step during sintering when ambient pressure is lower than the equilibrium CO pressure [17–19]. Thus, vacuum-sintering aids in the removal of binders and minimizes contamination during the burnout step, ensuring a cleaner final part with limited inclusion formation.

In recent research articles, shell printing has been explored in binder jetted materials. According to Frykholm et al. [20], the final relative density of binder jetted 316L stainless steel (SS) samples with a shell structure was higher than that of conventionally bulk binder jetted parts. They found that the shell-structured samples exhibited higher final relative density and improved tensile strength, which could be attributed to a lower pore fraction in the sintered parts. Miao et al. [8] conducted a study and discovered that there were variations in powder packing density between the bounded (shell structure) and unbounded (core) regions. This difference could be attributed to particle rearrangement that occurred between these two areas [21]. In binder jetting, a higher binder content, also known as binder saturation, leads to a longer debinding step required to remove the polymeric binder before the final sintering process [6,8]. Furthermore, the research indicated that the carbon content in sintered shell structured parts was significantly lower compared to the bulk printed parts [20]. Another study by Rahman et al. [9] focused on binder jet printing copper and revealed variations in densification, grain, and pore size between the shell structure and unbound areas. The traditional binding approach was found to enhance strength of the green part. However, it also hindered densification, limited grain coarsening, and caused appearance of remnant pores at the boundaries, in contrast to the shell printing methodology.

Although previous studies [8,9,20] have highlighted the advantages of shell printing, their primary focus was on analyzing densification and microstructure. Here, we aim to study the impact of binder and sintering atmosphere on microstructure-defect-property relationships. We hypothesize that (1) there are discrepancies in powder packing density and structure of as-printed parts between the shell and core regions, and (2) vacuum-sintering, with faster binder removal and densification, proves to be more efficient compared to H_2-sintering atmosphere. To test both

hypotheses, we will examine the powder packing density, resultant densified microstructure, and mechanical properties of both the shell and bulk binder jetted components.

2. Materials and methods

2.1. Powder processing

The gas-atomized 316L SS powder (with chemical composition of Ni=10.9 wt%, Cr=18.28 wt%, Mo=2.12 ,Mn=2.19 wt%, Si=0.58 wt%, C=0.03%, Fe=bal.) from Sandvik Osprey Company with particle size of -22 µm was used (see Figure 1A). Particle size distribution was found to be slightly different from the virgin powder in which the fraction of particles with size below 5 µm was lower in the recycled powder, as qualitatively seen in Figure 1A compared to our earlier work on the virgin powder published in [6]. The virgin powder has a particle size distribution (PSD) of d_{10} = 3.3 µm, d_{50} = 10.7 µm, d_{90} = 19.6 µm analyzed using a LS13 320 XR System. However, the used (or recycled) powder showed a slight increase in d_{10} and d_{50}. These powders have been recycled over time by blending used powder with virgin one at a ratio of 2:1 (used to virgin) every 10 cycles. The chemical analysis indicated that the recycled powder exhibited minimal deviation in terms of carbon and oxygen uptake compared to the virgin powder. This can be attributed to the storage of powder in a moisture-free environment and the adapted drying cycle applied to the powder before each printing session. The carbon (C), oxygen (O), nitrogen (N), and sulfur (S) concentrations in the recycled powder and sintered samples (shell and core) were quantified using LECO instruments (models TCH600 and CS744).

The binder jetted parts were manufactured using an Innovent$^+$ ExOne printer, employing optimized process parameters as reported in [6]. Two groups of coupons, each with dimensions of 15 × 20 × 10 mm, were fabricated. The first group was labeled as "bulk structure" and followed the conventional approach, with a polymeric binder (BA-005 water-based binder, ExOne, which works well with a variety of metallic materials) uniformly jetted onto the powder bed. The second group was termed "shell structure," and the fabricated parts relied on the binder jetted within the shell, with a certain thickness wall (ranging from 500-1000 µm), to provide strength to the green parts. The used layer thickness for printing was set at 50 µm which is about twice the biggest particles size [1]. A binder saturation of 80% was found to be sufficient for this powder and layer thickness. A 30-pL printhead was used for print. The powder bed temperature was maintained at 40 °C throughout the printing. The rollers and recoat speeds as well as the ultrasonic intensity were experimentally optimized [6] and set to be 600 rpm (smoothing roller speed), 300 rpm (roughing roller speed), and 400 mm/s (recoat speed). The applied drying time between each layer deposition was 10 s which was sufficient for both bulk and shell printed parts. The orientation of the printed parts was shown in Figure 1B. Tensile testing was conducted on dog-bone shell structured specimens, following the ASTM standard E8/E8M. The "shell" structured geometries were printed with a wall thickness of 1000 µm. This was attributed to enhanced part integrity, aimed at minimizing the risk of part collapse during depowdering and handling.

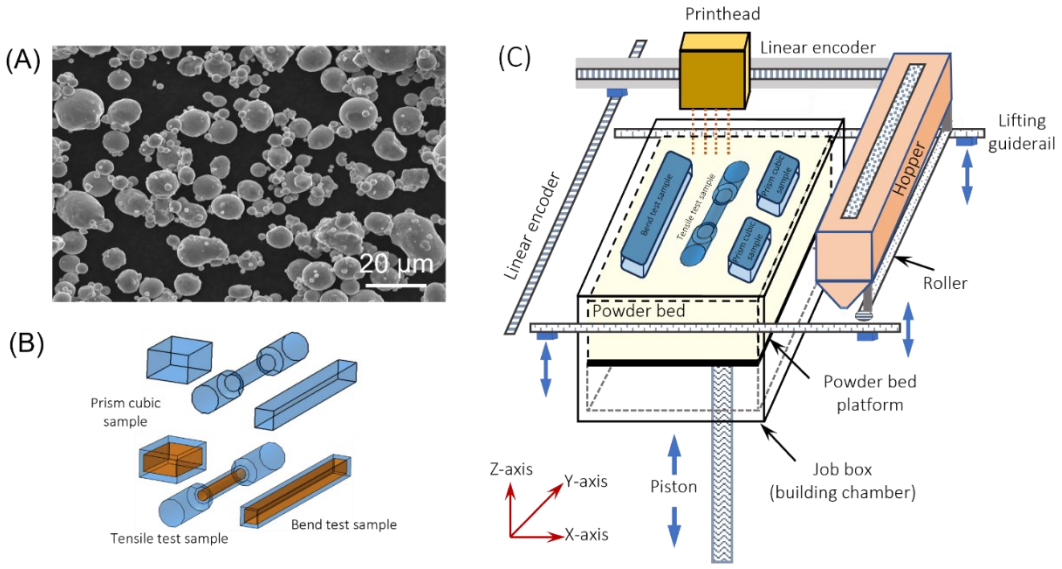

Figure 1. (A) SEM micrographs of the 316L SS recycled powders. (B) The designed bulk or shell-structured samples with specific dimensions and geometry. (C) An exemplary layout of the coupons and mechanical test specimens.

The binder jetted parts were cured at 185 ± 2 °C for 8 h. Then, the loose powder was removed using a brush. Sintering was performed in a tube furnace (Across International, model FT1700) with controlled heating and cooling rates of 5 °C/min. During the sintering, the parts were kept at 600 °C for 1 h to burnout the binder residue, after which the temperature was raised to 1400 °C and maintained for 2 h. The sintering, including the burnout step, was carried out under two different conditions: vacuum (10^{-5} bar) and ultra-high purity hydrogen with a constant gas flow rate of 50 ml/min. The purpose was to examine the impact of the atmosphere on densification and pore removal.

2.2. Characterizations

To quantify the powder bed uniformity and visualize in-process defects and anomaly formation, we employ an in-situ monitoring system through a collaborative research with Phase3D [22]. This system provides objective, uncertainty-quantified data from each layer of the powder bed. Unlike camera-only systems or diode-based monitoring, this technology uses two small sensor components and specialized software, retrofitted onto the powder bed without interfering with the printing process [23]. It employs rapid profilometry techniques to measure the height of exposed surfaces of powder-based AM parts before and after binder deposition for every layer. The hardware components consisted of a projector and a camera, where incident patterns were projected onto the exposed surface of the part, and the camera records their deformation to calculate the 3-D heightmaps of each layer. These heightmaps are sensitive to primary in-process part failure mechanisms (i.e., inadequate powder coating and out-of-plane part deformation). The heightmaps are an objective measurement, with real units of microns and can therefore be used to quantify observed anomalies, which can outperform camera-only subjective shadow analysis. Fringe Monitoring Software v1.01+ was used. To detect powder layer defects (PLDs), the camera

triggers measurements immediately after the powder spreading process, generating 3D heightmaps that are sensitive to striations, depressions, and clumping. Also, the imaging will be conducted after binder spraying and these two heightmap measurements will be compared to generate in-process defects visualization during binder-powder interactions with a 10 μm noise floor.

To compare quality of manufactured bulk and shell printed parts in the green state (after curing), micro-computed tomography (μ-CT) was performed using a ZEISS Metrotom 1500 model. The μ-CT study was conducted with parameters including an energy and current setting of 180 kV and 30 mA, using a Cu 0.5 mm filter, frame averaging over 3 frames, an angular span of 360° with a step increment of 0.08°, yielding a spatial voxel size of 5 μm. The acquired data underwent reconstruction and subsequent analysis using Volume Graphics Studio Max 2023.2.

To determine the part density after sintering, two methods were employed: the Archimedes' method according to the ASTM B962-17 standard and image processing to calculate the solid volume fraction. To prepare the samples for analysis, they were sectioned in the XZ direction, hot-mounted (MetLab phenolic thermosetting), and subjected to microscopy observations as described in [6]. Polished surfaces were examined using a digital optical microscope (Keyence VHX-7100) to analyze the fraction and pore distribution.

For the comparison of grain size between bulk and shell structured binder jetted parts, a scanning electron microscopy (SEM) system (JEOL 5900LV) was employed. To investigate the texture and grain size of the sintered parts, electron backscatter diffraction (EBSD) was conducted using an Oxford Instruments EBSD system at an acceleration voltage and step size of 20 keV and 0.75 μm, respectively and the data was post processed using MTEX. The sintered parts chemistry for C, O, N, and S was analyzed using LECO instruments (models TCH600 and CS744).

The Vickers microhardness test was performed according to the ISO 6507-1:2005 standard, applying a load of 300 g for a dwell time of 10 s. Mechanical tests, including tensile and bending experiments, were carried out using an MTS 880 machine. The tensile test (3 samples for each condition) involved a displacement rate of 0.0127 mm/s to determine yield stress, ultimate tensile stress (UTS), and elongation. The three-point bending test was carried out (5 samples for each condition) in accordance with the ASTM E290-14 standard. Both bulk and shell printing approaches were considered for three-point bending test and vacuum sintering was selected to achieve maximum relative density. The green parts with dimensions of 6.8 mm × 70 mm × 7 mm along (XYZ) were binder jetted and after sintering, the final dimensions were 5.54±0.07 mm × 70.00±0.40 mm × 5.59±0.09 mm (XYZ). The bending test was implemented in X and Z directions. The applied load and the resulting displacement were recorded throughout the test to calculate the flexural stress and strain using the following Eq. [24]:

$$\sigma = \frac{3Fl}{2bd^2} \qquad \text{(Eq. 1)}$$

$$\varepsilon = \frac{6Dd}{l^2} \qquad \text{(Eq. 2)}$$

where σ is the flexural stress (MPa), F is the applied force (N), L is the support span length (mm), b is the width of the specimen (mm), d is the thickness of the specimen (mm), ε is the flexural strain, and D is the deflection of the specimen (mm).

Fracture surfaces were examined using both a digital optical microscope (Keyence VHX-7100) and an SEM equipped with energy dispersive spectroscopy (EDS). The spatial distribution of pores was evaluated on one side of the failed tensile specimen using optical and SEM microscopes, as well as micro-computed tomography (μ-CT) analysis performed with a ZEISS Metrotom 1500 model.

3. Results and discussion

3.1. Qualitative analysis during binder jetting process and in the final printed parts

Figure 2 showed results of successfully deposited binder onto the powder bed and no PLDs were quantified during binder jetting of metal powders. The visual image (Figure 2-middle) demonstrated the deposited liquid binder onto the powder bed surface while possible displacement of powder due to binder bombardments was not obvious. The employed in-situ monitoring system enabled qualitative analysis in which powder-binder interaction occurred. It was observed that the binder deposition did not leave any powder layer defect (PLD) and proved homogenous binder/powder deposition in each discrete layer. Primarily, PLDs significantly contribute to defects in green parts, resulting in non-linear shrinkage and deformation of the sintered components, ultimately leading to costly part rejections. Indeed, inconsistencies during the powder spreading step can lead to non-uniform powder packing, causing variations in green density across different locations of the green part [25,26]. Consequently, the rate of shrinkage varies at these different locations, resulting in distortion. Our ongoing research aims to improve the resolution of the collected heightmap data to 1 μm, which will enhance our understanding of location-dependent defect formation in 3D printed parts. This will be achieved by increasing the focal length of the Phase3D Fringe monitoring system and developing a 3D reconstructed dataset, allowing us to compare in-process defect formation using this novel method with respect to μ-CT results.

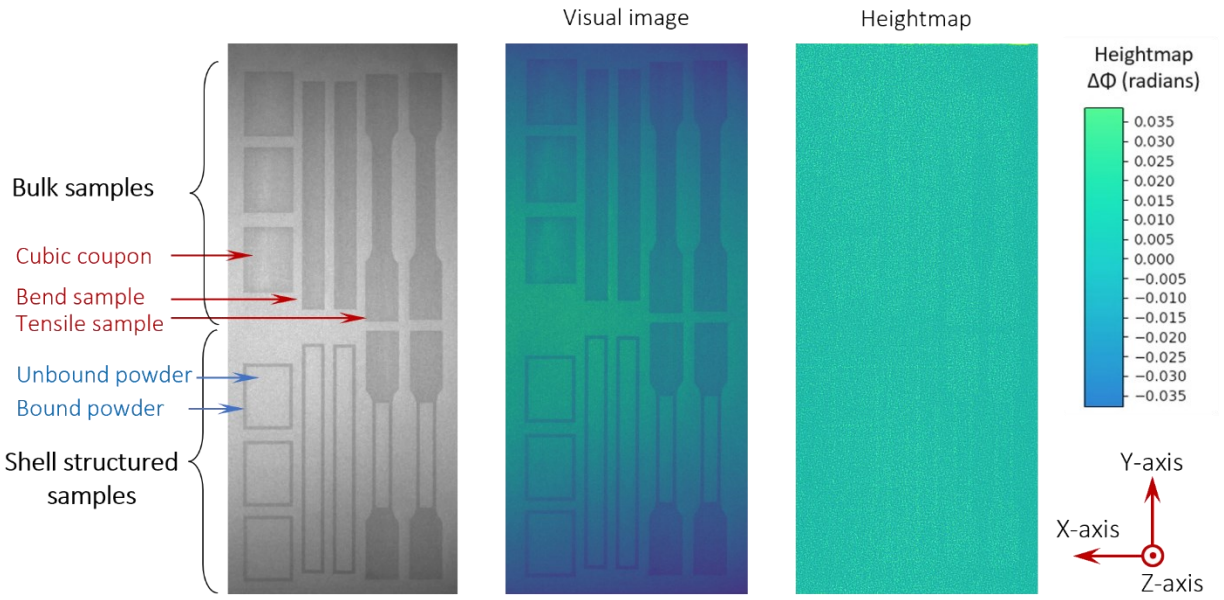

Figure 2. micrographs of a cross-sectional layer of printed parts showing bound (shell) and unbound (trapped powders at the core) regions. Three types of specimens including cubic coupons, Charpy and tensile samples were binder jet printed. The heightmaps micrograph shows minimal powder displacement during binder-powder interactions indicating uniformity in each discrete layer. ΔΦ in the heightmap is a difference in radians from the expected values of the carrier phase map.

During the process of jetting binder onto the powder bed, the droplets' ballistic effects and the displacement/rearrangement of small particles on the top surface of each layer can create gaps in the regions exposed to the liquid binder [21,27]. Based on previous knowledge, it was believed that particle bonding induced by surface tension would result in higher green density in the bulk binder jetted parts. However, our recent findings contradict this prior understanding [9]. In essence, the impact of droplets on the powder bed during binder-powder interaction may have led to the formation of craters, ejection of particles, and rearrangements. However, in the core (or unbound region) of the shell printed parts, the powder is more densely packed, resulting in a higher green density in that area. Examples of shell printed vs. traditional binder jet pattern printed parts were shown in Figure 3. Using μ-CT analysis, it was found that the green density was enhanced up to 5% suggesting the unbound powders were packed more than the bound particles in the shell structured sample.

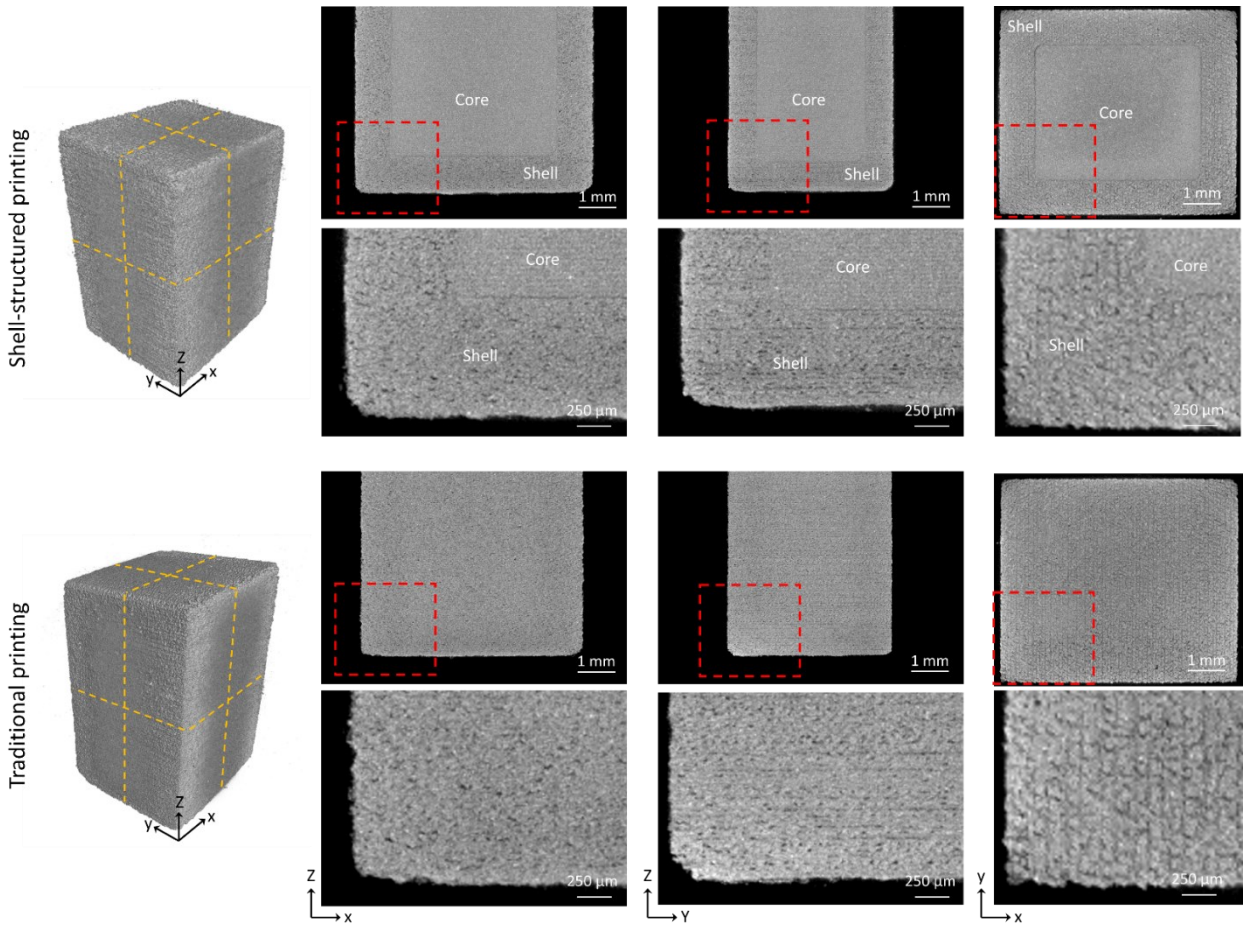

Figure 3. Shell vs. traditional printing. In-process line defects were visible on the 2D projected µ-CT micrographs in which binder was jetted onto the powder bed to make an object with dimensions of 6 mm × 4 mm × 8 mm (shell wall thickness of 1 mm). Sections were made based on the yellow dash lines on each plane.

3.2. Densification behavior and microstructure analysis

Green density - Shell printing is considered a novel approach because it leads to higher green density, which in turn results in lower shrinkage and reduces the risk of powder contamination by elements such as C, N, O, and S—major components present in the liquid binder. The measured green density of the binder jetted samples (results were given in Table 1) indicated that when a bulk structure was manufactured, the density reached ~50%. On the other hand, using shell printing resulted in a higher green density of 54% for parts with a shell wall thickness of 500 µm. It is worth noting that the 316L SS powder used in this study was not virgin but rather continuously recycled for a period of 1 year. The SEM micrograph of the recycled powder showed lower fraction of ultra-fine particle (<5 µm). As a result, the relative density of the green part in this study was lower compared to other reports in [6], where virgin powder was used, and a relative density of ~52.5% was achieved.

During binder jetting, the ballistic effects of droplets and the rearrangement of small particles on the powder bed can create gaps in liquid-exposed areas [21,27]. Traditionally, it was believed that surface tension-induced particle bonding would lead to higher green density in bulk binder jetted parts [21]. The hypothesis proposes that droplet impact may form craters, eject particles, and cause rearrangements, contradicting the assumption of higher density. Hence, it was anticipated to achieve a higher green density in the shell printed part with a wall thickness of 500 µm. However, part integrity and green strength must also be considered when manufacturing a shell structure using binder jetting. It was noticed that the 3D printed parts with a shell thickness of 500 µm were fragile in their green state, necessitating a higher shell thickness for producing parts with greater mass.

Table 1. The analyzed data presents the green density of the binder jetted parts after curing, the sintered relative density obtained through Archimedes and optical image analysis, and the shrinkage observed in both bulk and shell printed structures sintered under vacuum or H_2 atmosphere. In the optical image analysis, the terms "shell" and "core" refer to the "bound" and "unbound" regions, respectively. The reported relative density values are derived from 3 measurements in the core and 24 measurements in the shell regions.

Samples	Green density (%)	Shell thickness after sintering (µm)		Sintered density by optical image analysis (%)				Shrinkage (%)					
		Vacuum	H_2	Vacuum		H_2		Vacuum			H_2		
				Shell	Core	Shell	Core	X	Y	Z	X	Y	Z
Shell - 500 µm	54.0±0.1	409	426	99.7±0.1	99.2±0.3	95.6±2.4	98.5±0.3	18.2	18.4	19.4	16.8	17.2	18.9
Shell - 750 µm	53.5±0.1	596	681	99.7±0.1	99.3±0.1	97.0±1.7	98.8±0.2	18.6	18.6	19.6	17.5	17.5	19.6
Shell - 1000 µm	53.2±0.1	817	919	99.7±0.1	99.2±0.3	95.7±2.2	98.3±0.3	18.8	18.6	20.2	17.4	17.5	19.5
Bulk	50.0±0.1	---	---	99.0±0.2		96.4±1.5		19.2	19.0	21.9	18.5	17.9	20.7

Linear shrinkage - To investigate the impact of the binder on linear shrinkage, both bulk and shell printed samples were sintered under two atmospheres, vacuum and H_2. In any sample, the shrinkage was found to be higher in the vacuum-sintered condition compared to the H_2-sintering atmosphere, resulting in higher final relative density for the vacuum-sintered specimens. The bulk binder jetted components, where the binder is uniformly deposited throughout the part volume, displayed shrinkage behavior consistent with earlier studies [6,27,28]. These studies proposed that the order of linear shrinkage was Z (build direction axis) > X (powder recoating direction) > Y (print head traverse axis). Despite Rahman et al.'s findings [9] that parts with thinner shell thickness showed higher shrinkage, as the unbound powder densified more than the bound powder. This observation might be attributed to the choice of material used for binder jetting.

In the case of copper, carbon residue from the binder tends to have minimal diffusion [9], whereas in iron, it can function as an interstitial alloying element, diffusing from the powder surface into the grains [29]. Additionally, carbon can lower the solidus temperature of iron, making the densification process easier. The packing density of the packed loose powder (unbound) is typically higher than that of the binder jetted regions. Consequently, in our study, increasing the shell thickness is more likely to result in higher shrinkage in the X and Y directions. Interestingly, we observed that the difference in linear shrinkage between X and Y could be reduced when the

powder packing density and resultant green density decreased in the recycled binder jetted powder. However, in the Z direction, as the liquid binder is burned out, the pores at the layer interfaces collapse under the influence of gravity, leading to higher shrinkages compared to the X and Y directions.

Densification - The densification behavior of the sintered binder jetted 316L SS powder was investigated to understand the role of binder impact and sintering atmosphere on pore removal and final density. The optical micrographs in Figure 4 display the sintered microstructure of both the shell (bound) and core (unbound) regions, along with the morphology and distribution of pores. A clear variation in pore microstructure can be observed between the bound and unbound areas, which are indicated by the dashed red line. It was observed that the pores, if any, were uniformly distributed throughout the cross-section of the vacuum-sintered specimens, where the relative density exceeded 99.3%. In contrast, the H_2-sintered specimens displayed a higher fraction of pores on the printed shell wall (bounded powder) compared to the core (unbounded powder), with relative densities of ~96% and 98.5%, respectively. The measurements of the bounded wall thickness for all the shell printed samples (see data in Table 2) revealed that the vacuum-sintered specimens had smaller wall thickness compared to the H_2-sintered specimens, corroborating with the linear shrinkage values.

In the core region (unbound particles), densification was significant, as indicated by the higher relative density observed in the vacuum-sintered sample compared to the H_2-sintering atmosphere. This was evident from the presence of isolated, fine, spherical pores. The core, which was devoid of binder, experienced tight packing during the powder spreading process, with the outer shell encompassing it. Consequently, the particles primarily had to navigate the gaps between them to establish connections and achieve densification by closing the pores. While a few pores persisted, the majority of these remaining pores underwent a transformation, becoming more rounded and diminishing in size. The average pore size in the unbound regions of both the vacuum-sintered and H_2-sintered specimens was measured to be 3.3 ± 1.5 μm and 4.5 ± 1.8 μm, respectively. In vacuum-sintered specimens, the pore circularity and maximum pore size were 0.96 and 10.9 μm, while in H_2-sintered specimens, they were 0.93 and 26.6 μm, respectively.

On the other hand, the bound region in H_2-sintered specimens showed a significant amount of interconnected, irregularly shaped, coarse pores which were unevenly distributed. The existence of these large and irregularly shaped pores suggests an inadequate formation of necks between the particles. It is possible that sub-surface pores formed during binder droplet impact with the powder bed during binder deposition (see Figure 3), thus, hindered neck formation during sintering. In other words, the interaction between the powder and binder results in the creation of subsurface pores within the printed parts, potentially causing a visible continuous gap between the printed layers. Interestingly, the pore size in the unbound regions was found to be ~3.5-4 μm regardless of the sintering atmosphere, suggesting that the green density of the unbound packed powder was high enough, and sintering effectively eliminated the majority of pores.

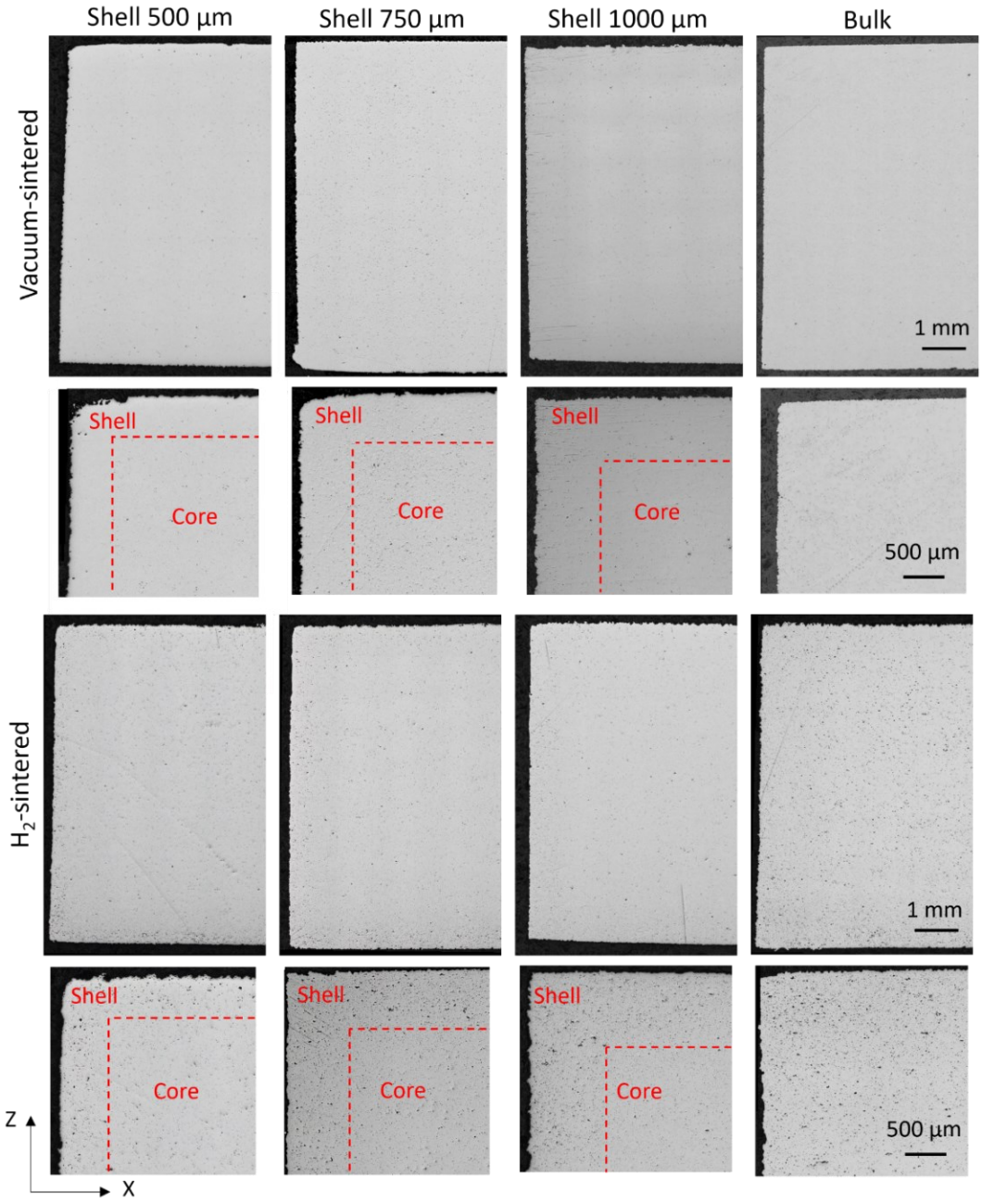

Figure 4. The optical micrographs display the XZ cross-section of the sintered binder jetted 316L SS samples. The red dash lines mark the boundaries between the shell wall and the core in the shell structured specimens.

Table 2. Grain and pore analysis on the EBSD micrographs shown in Figure 5.

	Bulk sample		Shell sample - unbound		Shell sample - bound	
Sintering condition	Vacuum	H_2	Vacuum	H_2	Vacuum	H_2
Grain size (µm)	35.1±23.7	32.3±16.1	32.2±16.4	36.7±16.1	33.1±18.2	26.1±12.9
Pore size (µm)	3.5±1.9	7.1±4.2	3.3±1.5	4.5±1.8	3.1±2.3	8.2±3.1
Max pore size (µm)	13.3	24.7	10.9	26.6	15.4	22.5
Pore circularity	0.92	0.91	0.96	0.93	0.90	0.88

Grain and pore analyses - Figure **5** presents EBSD micrographs taken at the cross-section surface of both bulk and shell structured specimens sintered under vacuum or H_2 atmosphere. The band contrast micrographs revealed a relatively uniform microstructure and grain distribution in the vacuum-sintered specimens, with mean grain sizes of 35.1 µm, 32.2 µm, and 33.1 µm for the bulk, unbound-shell, and bound-shell structured samples, respectively. Notably, a difference in mean grain size was observed between the bound and unbound regions of the H_2-sintered shell structured samples, with the grain size measuring 36.7 µm in the unbound area and 26.1 µm in the bound area. This disparity could be attributed to the presence of porosity in the bound region, which hindered grain coarsening and led to the formation of smaller grains in the final sintered microstructure. Rahman et al. [9] previously hypothesized that the presence of C residue from binder burnout in the bound region of binder jetted copper powder could retard grain growth, as copper does not dissolve C in its crystal structure. This is due to the fact that solubility limit of C into Cu is ~0.04 at.% [30]. However, in our study, C diffusion in iron makes this explanation less likely for the remnant pores observed. As explained earlier, particle rearrangement and the resulting lower relative density in the bound area were identified as the main factors contributing to this behavior. In contrast, the vacuum-sintered sample showed no significant difference between the two regions, indicating effective densification and pore removal when high vacuum conditions were applied during the sintering of binder jetted samples.

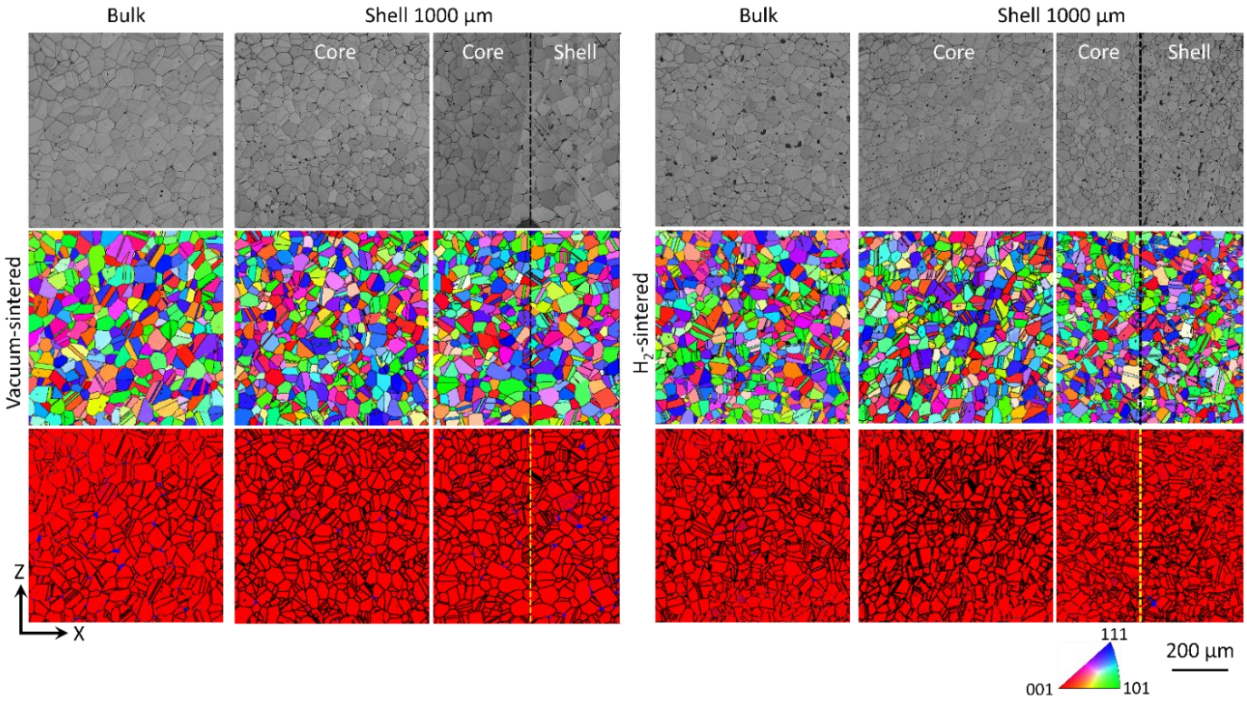

Figure 5. Electron backscattered diffraction micrographs: (top) band contrast, (middle) inverse pole figure (IPF), and (bottom) phase map results taken from the vertical cross-section of the bulk or shell structured binder jetted 316 L SS alloy. In the phase map micrographs, austenitic grains are in red, and delta-ferrite are in blue at the grain boundaries.

Elemental analyses – The concentration of C, O, N, and S is crucial for densification during sintering, evolution of microstructure, and mechanical behavior and measurements were conducted on samples and results were summarized in Table 3. The elemental analysis indicated that in the virgin powder, C, O, and N were 0.025, 0.129, and 0.113 wt%, respectively. These values slightly increased in the recycled powder to 0.029, 0.141, and 0.121 wt%, respectively. Binder jetting and curing of the 3D printed parts from the recycled powder showed a slight deviation compared to the virgin powder. Binder burnout during sintering at 1400 ℃, especially under vacuum, effectively reduced these elements, approaching the levels in the virgin powder. This reduction suggested the efficiency of vacuum-sintering in removing C and O. In general, the increase after binder jetting was attributed to the polymer binder, while the reduction during sintering resulted from binder burnout and potential decomposition/desorption of C, N, and O-rich layers on the particle surfaces. These observations agreed with earlier works in [5,6,31].

Table 3. Elemental analysis including C, O, N, and S content of the recycled powder, cured, and sintered samples in [wt%]. Results were also compared with virgin powder, cured, and sintered samples [6].

Samples	Carbon	Oxygen	Nitrogen	Sulfur
Virgin 316L SS powder [6]	0.0250	0.1290	0.1130	0.0068
Recycled 316L SS powder	0.0291	0.1407	0.1210	0.0072
Printed and cured parts made from virgin powder [6]	0.2200	0.2720	0.1560	0.0060
Printed and cured parts made from recycled powder	0.2290	0.2870	0.1590	0.0059
Vacuum-sintered (virgin powder) – bulk [6]	0.0267	0.0072	0.0016	0.0054
Vacuum-sintered (recycled powder) – bulk	0.0268	0.0082	0.0010	0.0051
Vacuum-sintered (recycled powder) – unbound region	0.0259	0.0081	0.0011	0.0049
H_2-sintered (recycled powder) – bulk	0.0307	0.0087	0.0013	0.0057
H_2-sintered (recycled powder) – unbound region	0.0267	0.0081	0.0014	0.0052

The sintering for binder jetted metals can be performed under various conditions, including vacuum, inert gas, or reducing atmosphere. However, each atmosphere has its own advantages and challenges. For instance, using N_2 or Ar may lead to the absorption of nitrogen by iron, forming nitride and negatively affecting the mechanical properties. Moreover, there is a possibility that Ar may become trapped within the pores, potentially impeding the densification process during the final stages of sintering. On the other hand, H_2, a reducing atmosphere, is suitable for active metals such as copper but can create issues with trapped H_2O during sintering, hindering the final stage of the process. The small size of hydrogen atoms enables them to diffuse the metal lattice, impeding the removal of remaining porosity [32,33]. Finally, this hydrogen diffusion poses a risk of hydrogen embrittlement [34,35], potentially resulting in reduced ductility and structural integrity over time.

To facilitate densification, vacuum sintering is the favored choice for binder jetted metals. This method not only reduces the occurrence of gas-filled pores and oxidation but also limits C contamination [11]. During vacuum sintering, a significant reduction in the sintering rate is

observed during the final stages, and pore healing takes place through lattice diffusion of vacancies, a process governed by the Nabarro-Herring mechanism [12,13]. However, it is important to consider that for metals such as 316L SS, the applied temperature of sintering can lead to supersolidus liquid phase sintering (SLPS), where liquid metal accelerates the densification rate, provided there are no gas pores within the particles. One potential drawback of vacuum sintering is the possibility of evaporation of alloying elements such as Cr in 316L SS, which can accelerate the evaporation-condensation process and lead to unintended consequences such as corrosion resistance reduction. This would be adjusted in feedstock developed for binder jetting process. Nonetheless, vacuum sintering remains effective in removing excessive C introduced by the polymer binder into the printed 316L SS components. The observed pattern in relative density of sintered parts suggests that reducing binder content is advantageous for enhancing part densification.

3.3. Mechanical properties

Microhardness results (see Table 4) indicated that the average hardness values of the vacuum-sintered specimens were between 130-135 $HV_{0.5}$ while it was higher in H_2-sintered samples about 135-145 $HV_{0.5}$. Also, a comparison was made between microhardness values of the bulk and shell structured regions and results were shown in Figure 7. These values were in agreement with the literature [6,10,16,36]. The higher microhardness values observed in the cast and wrought 316L SS alloy may be attributed to differences in grain structure and phases compared to the sintered-based 3D 316L SS alloy [37].

Tensile tests were conducted on both bulk and shell structured binder jet printed 316L SS specimens to assess the stress and ductility when employing the new binder jet strategy and the results were presented in Figure 6. Table 4 summarizes the yield strength (YS), ultimate tensile strength (UTS), and elongation (%) for comparison with traditionally manufactured or 3D printed 316L SS alloy. It is evident that when vacuum-sintering condition was used for densification, the strength and ductility was nearly equivalent in both bulk and shell printed samples, e.g., YS = 202 MPa, UTS = 545 MPa, and ε = 70% (which is a comparable elongation compared to the reported values for 316L SS ranging 50-75%, see Table 4). However, when the H_2-sintering atmosphere was employed, it resulted in significantly reduced ductility and tensile strength in both bulk and shell printed parts. A marginally reduced elongation in vacuum-sintered, shell-printed samples compared to the bulk printing condition may be attributed to a slightly higher fraction of pores in the shell, leading to potential crack initiation at the bound-unbound interface, as depicted in µ-CT micrographs in Figure 10B. Micrographs illustrating the spatial distribution of pores (second column) reveal internally connected longitudinal pores or gaps (in red color) post-tensile test, substantiating our hypothesis of crack initiation at this interface and lowering elongation.

The mechanical properties of sintered 316L SS are affected by three key factors: porosity morphology and its size, grain size, and phase fraction (austenite and δ-ferrite), with increasing sintering temperatures leading to improved properties [38]. Our observations indicated that the choice of binder jetting strategy and sintering atmosphere had effects on densification and pore removal. Optical micrographs presented in Figure 4 demonstrated that vacuum-sintering led to a more uniform microstructure with a relative density of 99.0% and higher in both bulk and shell structured parts. In contrast, remnants of pores were observed in the H_2-sintered specimens, especially in areas where the binder was jetted onto the surface (bounded regions in both shell structure and bulk specimens). N. Kurgan [39] demonstrated that the mechanical strength of sintered 316L SS manufactured through powder metallurgy is inversely related to porosity, as sintering conditions can directly alter pore size and shape. Pores can cause localized stress concentration, resulting in earlier onset of plastic deformation at lower stress levels. Muterlle et al. [40] highlighted that the introduction of a small fraction of δ-ferrite (up to 4%) in 316L SS, manufactured through metal injection molding (MIM), contributed to enhanced YS, UTS, and notably, ductility. Similarly, in our study, we observed an increase in both YS and UTS, accompanied by a substantial improvement in elongation. Comparing the elongation of 316L SS fabricated through non-beam-based AM processes (see Table 4), the binder jetting method achieved ~40% higher ductility, which can be explained by the increased presence of annealing twins in the microstructure of the sintered parts, as opposed to the casted or wrought alloy [41]. The side view of fracture surfaces in vacuum-sintered specimens displayed necking, indicative of a shear fracture, along with typical dimples characteristic of ductile fractures [16,33]. The entire fracture surface of the vacuum-sintered part exhibited dimples, and no features related to the δ-ferrite phase were observed. A closer examination revealed a higher concentration of dimples at the center of the fracture surface, while shallower parabolic dimples [42], a result of higher shear loading on the edges, were evident. No second-phase particles were observed at the center of these dimples. In contrast, H_2-sintered samples lacked necking, suggesting low elongation. This issue could be associated with higher concentration of hydrogen in H_2-sintered specimens, leading to the hydrogen embrittlement and reduction of ductility [34,35]. The fracture surfaces of the H_2-sintered samples displayed a combination of dimples and voids, indicating the presence of pores in the shell region (see Figure 9B).

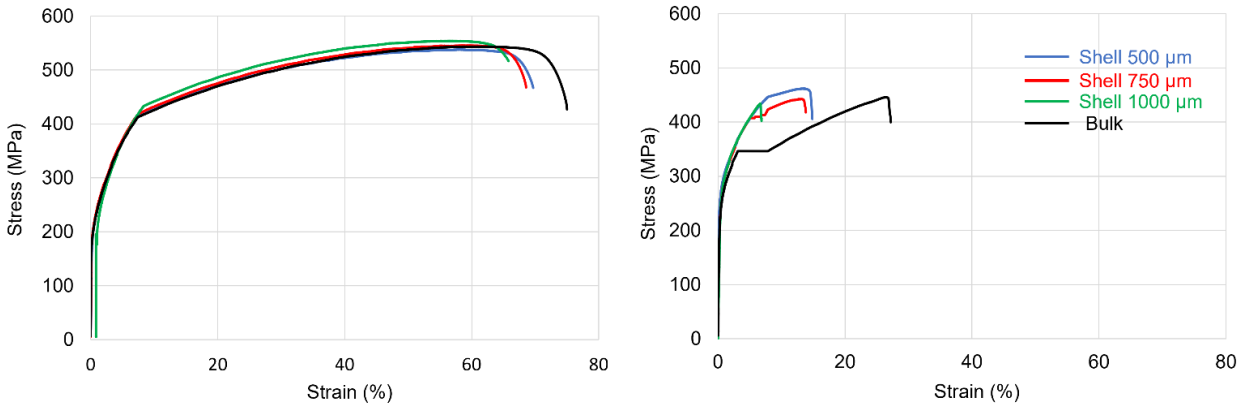

Figure 6. Stress-strain curves of the (left) vacuum-sintered and (right) H_2-sintered binder jetted 316L SS samples.

Table 4. Summary of tensile test results and microhardness measurements compared to literatures.

Samples	Sintering temperature and time	Yield stress (MPa)		Ultimate tensile stress (MPa)		Strain (%)		Microhardness ($HV_{0.5}$)		Ref.
		Vacuum	H_2	Vacuum	H_2	Vacuum	H_2	Vacuum	H_2	
Shell - 500 µm	1400 °C - 2 h	201.7	284.3	549.0	461.5	65.8	14.8	133.1±4.2	147.2±10.4	This study
Shell - 750 µm	1400 °C - 2 h	202.3	284.7	543.6	430.7	68.5	13.9	135.4±2.9	145.3±2.7	
Shell - 1000 µm	1400 °C - 2 h	201.9	284.9	543.4	427.2	69.2	7.7	134.5±3.1	137.0±11.7	
Bulk	1400 °C - 2 h	202.3	284.7	545.1	444.1	75.3	27.1	128.5±2.6	135.9±3.1	
Shell	1360-1380 °C - vacuum + Ar	175	---	528	---	57	---	112		[20]
Bulk		170	---	511	---	58	---	108	---	
Bulk	1400 °C - 2 h	201.9	---	573.4	---	90.3	---	132.0±7.0	---	[6]
Bulk	1360 °C - 3 h	176.0	---	535.0	---	49.0	---	148.0±11.0	---	[10]
Bulk	1380 °C - 2 h	191.0	---	544.0	---	73.0	---	138.0±4	---	[16]
Bulk	1380 °C - 2 h	---	189-198	---	534-558	---	64-80	---	---	[43]
Bulk	1395 °C - 1.5 h	---	---	---	518.0	---	61.9	---	---	[44]
Bulk	n/a	214	---	517	---	43	---	119	---	[36]
Fused filled filament	1380 °C - 3 h	155-165	---	500-520	---	32 - 37	---	---	---	[45]
Extrusion 3D printing	1350 °C - 2 h	166	---	524	---	96	---	---	---	[42]
Metal injection molding		175	---	520	---	50	---	130	---	[36]
Cast		310	---	620	---	50.0	---	185	---	[37]
Wrought		170	---	425	---	40	---	210	---	[37]
AISI 316L SS		170	---	485	---	60	---	---	---	[46]

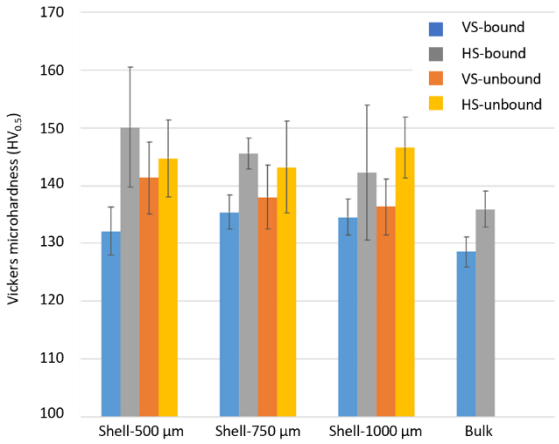

Figure 7. Microhardness values from bulk and shell printed parts collected at shell and core regions. "VS" refers to vacuum-sintering and "HS" refers to H_2-sintering.

Three-point bending tests were performed on vacuum-sintered 316L SS samples, encompassing both bulk and shell structured configurations, to evaluate their bending behavior. The flexural stress-strain curves were illustrated in Figure 8, and their outcomes are briefly presented in Table 5. The bending curves revealed distinct stages of elasticity and plasticity across all the tested samples. Notably, the results demonstrated that the maximum bending strength was higher in the Z direction for both the bulk and shell structured samples when compared to the X direction. Importantly, none of the bent samples exhibited any cracks, emphasizing the favorable plasticity of the 316L SS alloy produced through binder jetting.

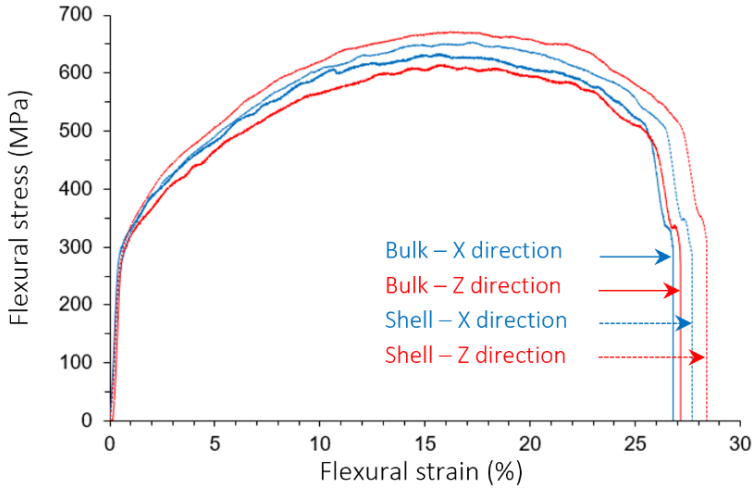

Figure 8. Stress-strain curves of the (left) vacuum-sintered and (right) H_2-sintered binder jetted 316L SS samples.

Table 5. A summary of three-point bending test results of the binder jetted bulk or shell structured 316L SS samples compared to literatures.

Samples	Yield bending stress (MPa)	Maximum bending stress (MPa)	Ref.
Shell – X direction	310±6	612±3	This study
Shell – Z direction	319±5	672±3	
Bulk – X direction	312±9	620±13	
Bulk – Z direction	307±8	654±9	
Bulk – X direction	343±6	618±7	[47]
Bulk – Y direction	337±3	601±4	
Bulk – Z direction	332±4	588±4	

Fractographic analysis was performed on the specimens post-tensile testing, and representative micrographs of the fracture surfaces were presented in Figure 9. The micrographs (Figure 9B) of the H_2-sintered samples indicated minimal necking, suggesting a fracture surface with low ductility, possibly involving a mixed brittle-ductile fracture failure mechanism because of the significant pore percentage in both the bulk and shell structured regions, leading to early failure at lower elongation. Remnant pores in the microstructure exerts a negative impact on both yield strength and ductility, which can be attributed to the decreased load-bearing area and the stress concentration around each pore. SEM observations at higher magnification around pores showed slight plastic deformation with numerous shallow dimples, which could be linked to the premature failure in specimens sintered at lower temperatures. On the contrary, fractography on the fracture surface of the vacuum-sintered samples displayed dimples (free of any second-phase particles), suggesting ductile fracture (see Figure 9A). The high elongation observed in the vacuum-sintered samples was linked to the work hardening in 316L SS, primarily driven by twinning and cross-slip mechanisms, resulting in increased dislocation density and improved ductility [6,48].

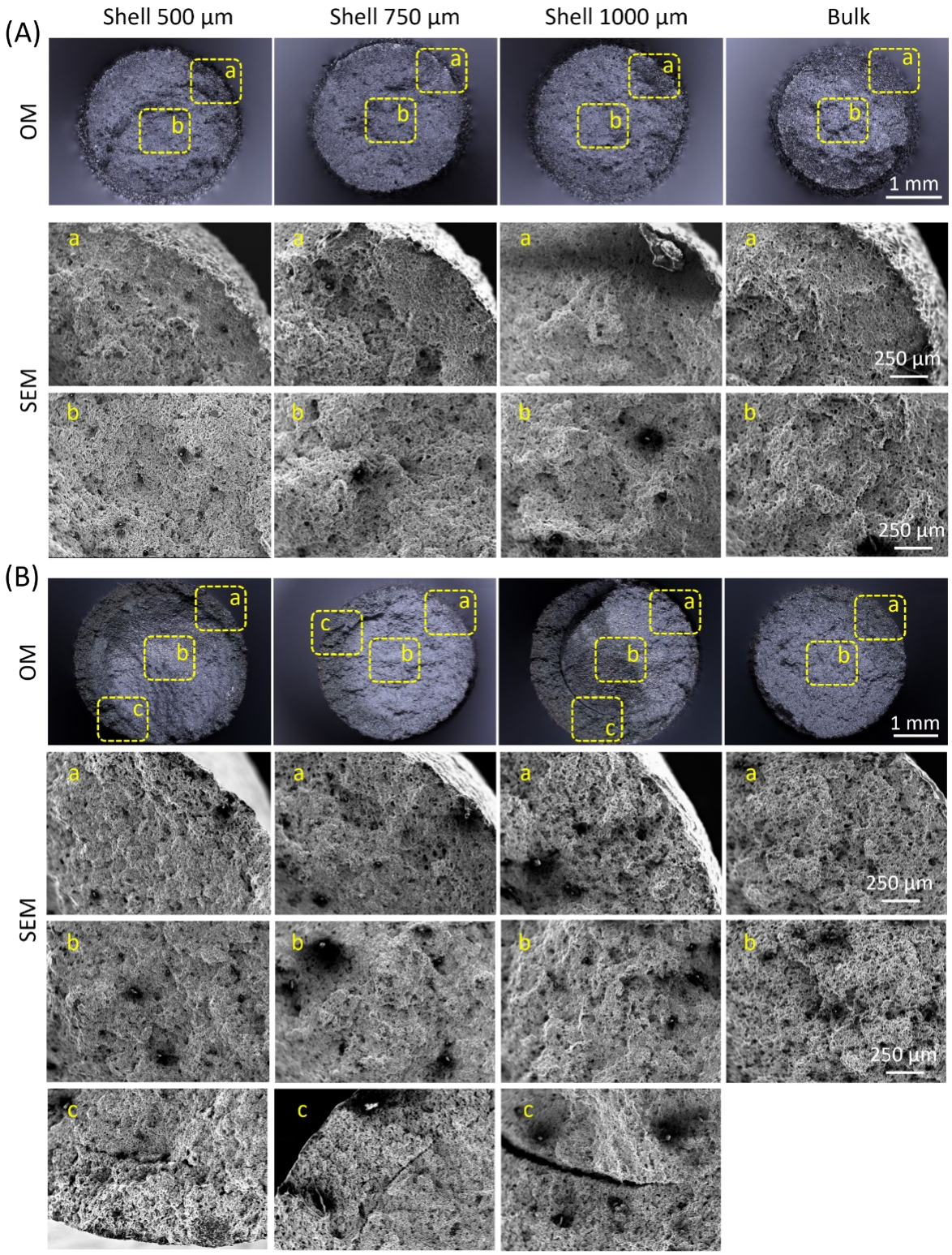

Figure 9. Fractography analysis: optical and SEM micrographs taken from (A) vacuum-sintered and (B) H_2-sintered binder jetted 316L SS samples.

3.4. Micro-computed tomography on failed tensile specimens

Figure 10 illustrates the distribution of pores conducted via μ-CT on the tensile specimens after failure. In the vacuum-sintered part, the fracture surface exhibited clear signs of ductile fracture, characterized by dimples, while the H_2-sintered samples displayed brittle fracture tendencies. Most of the observed voids were in proximity to the fracture surface of the vacuum-sintered part. These voids, often ellipsoidal in shape, tended to align with the tensile direction, with their density increasing closer to the fractured surface. The defect fraction was measured in the failed fracture surfaces showing pore fraction of 0.92% and 0.67% in the bulk and shell structured vacuum-sintered samples, respectively, after tensile test, while these values were to 4.09% and 4.01% in the H_2-sintered samples. It is important to highlight that all samples were positioned on the XY plane during the sintering process. Notably, in the case of the H_2-sintered samples, it was observed that the side in contact with the crucible exhibited a greater pore fraction, particularly within the range of 0.8-1.0 mm from the bottom face. This observation suggests that air or residual burnt binder may have become trapped in the H_2-sintered samples, consequently impacting their tensile behavior adversely. Specifically, in the H_2-sintered shell structured sample, there was an observation of detachment between the shell region and the unbound area.

An earlier investigation by Jamalkhani et al. [6] uncovered that grain boundary regions abundant in delta-ferrite experienced a higher concentration of strain, leading to increased void nucleation. This phenomenon was attributed to the superior strength of delta-ferrite compared to austenite (in grain), as well as its body-centered cubic crystal structure, which possesses fewer active slip systems compared to the face-centered cubic crystal structure in austenite. Consequently, void nucleation and growth were observed in areas containing delta-ferrite along grain boundaries. In terms of void growth, under triaxial stress conditions, voids tended to grow rapidly in the direction of tension, as evident in the necked tensile specimen of vacuum-sintered samples. Moreover, voids exhibited a propensity to grow and eventually coalesce perpendicular to the direction of tension, leading to crack formation and eventual failure. Additionally, the 2D shadow projection on the XY plane revealed deformation bands along the fracture surface of the vacuum-sintered samples, forming at a 45° angle from the tensile axis, with central cracking observed. However, the fracture surface was perpendicular to tension in H_2-sintered samples and surface cracking was also seen on the right side of the 2D shadow projection on XY plane.

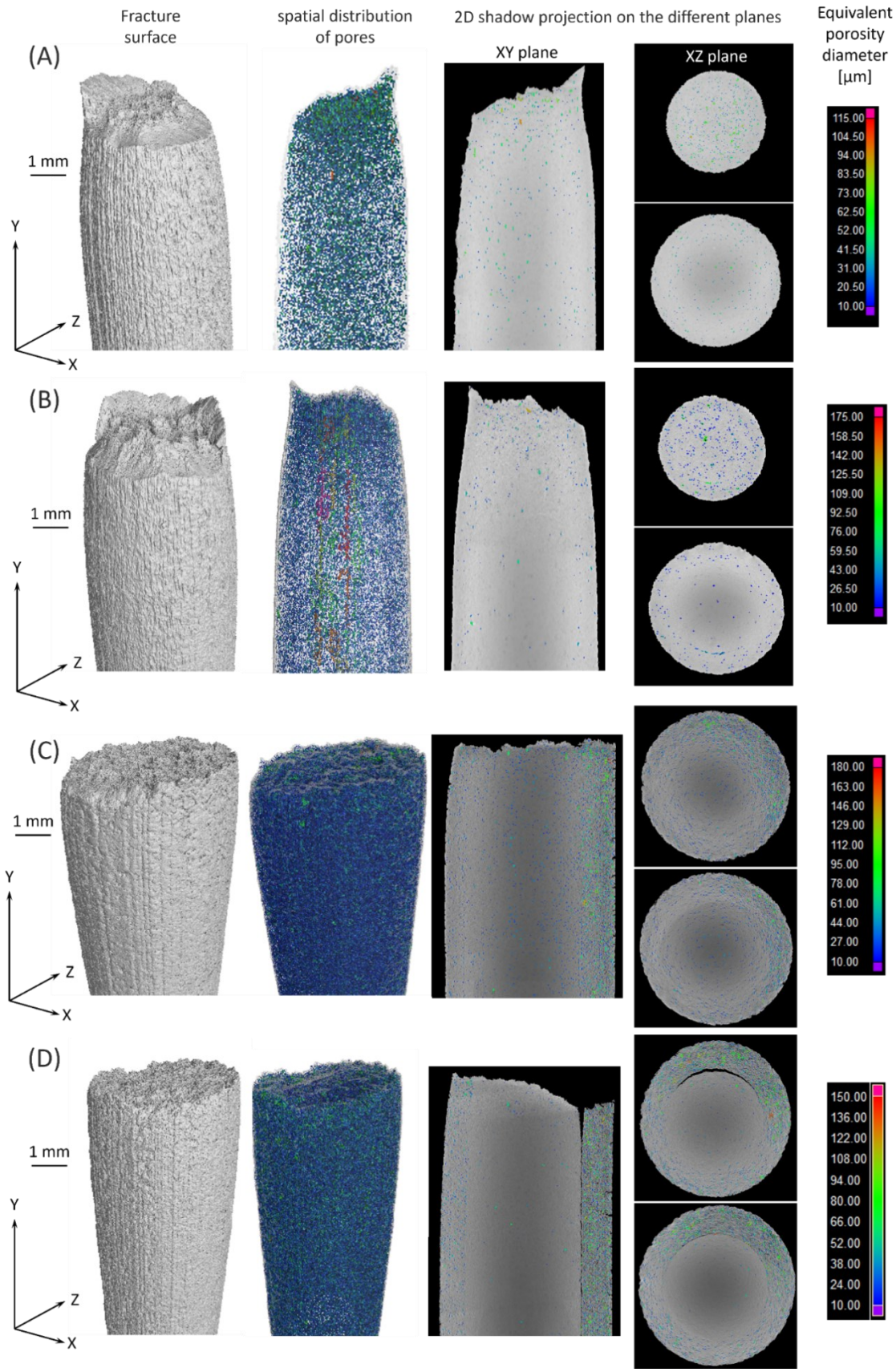
Fracture surface
spatial distribution of pores
2D shadow projection on the different planes
XY plane
XZ plane
Equivalent porosity diameter [μm]
(A)
1 mm
Y
Z
X
115.00
104.50
94.00
83.50
73.00
62.50
52.00
41.50
31.00
20.50
10.00
(B)
1 mm
Y
Z
X
175.00
158.50
142.00
125.50
109.00
92.50
76.00
59.50
43.00
26.50
10.00
(C)
1 mm
Y
Z
X
180.00
163.00
146.00
129.00
112.00
95.00
78.00
61.00
44.00
27.00
10.00
(D)
1 mm
Y
Z
X
150.00
136.00
122.00
108.00
94.00
80.00
66.00
52.00
38.00
24.00
10.00

Figure 10. μ-CT outcomes depicting the fracture surface of the failed tensile samples, spatial distribution of pores within the fractured part post-tensile testing, and 2D shadow projections on the XY and XZ planes demonstrating the distribution and dimensions of pores within the fractured tensile specimen. (A,B) Vacuum-sintered and (C,D) H_2-sintered samples. (A,C) bulk and (B,D) shell structured specimens.

3.5. Possible challenges in traditional printing vs. shell printing

While the binder plays a crucial role in bonding particles and defining the shape of the printed part, it has a detrimental impact on densification [9]. This is because it reduces the initial density of the green part and introduces a higher proportion of pores in the as-printed components. Essentially, the presence of the binder leads to increased porosity in the binder jetted parts, which becomes challenging to eliminate during the sintering process. If binder residue hinders grain growth during sintering, it can cause a delay in both densification and grain coarsening, particularly in parts with higher binder saturation. For large and intricate binder jetted parts, relying solely on thin shell wall printing may not suffice. Our μ-CT observations revealed the potential for cracks to form between the upper overhang structure and the underlying unbound powders in the green components (as shown in the example in Figure 11A). Should such cracks develop in binder jetted green parts, they will not completely close during the sintering process, ultimately reducing the mechanical properties of the part (see sections 3.3 and 3.4). Also, the mechanical testing results showed that a marginally reduced elongation in vacuum-sintered, shell-printed samples compared to the bulk printing condition may be attributed to a slightly higher fraction of pores in the shell, leading to potential crack initiation at the bound-unbound interface, as depicted in μ-CT micrographs in Figure 11B. Micrographs illustrating the spatial distribution of pores reveal internally connected longitudinal pores or gaps (in red color) post-tensile test, substantiating our hypothesis of crack initiation at this interface and lowering elongation. Consequently, future research will focus on evaluating the strength of green parts, and if necessary, explore Design for Additive Manufacturing (DfAM) strategies to address the trade-off between improved properties in the sintered part and reduced strength in the green part. To achieve the enhanced properties offered by the shell printing approach, careful part design will be essential to minimize issues like slumping in overhang features. Additionally, further investigation into the impact of different binder types will contribute to our understanding of DfAM strategies aimed at minimizing binder usage while maximizing green part strength through shell printing.

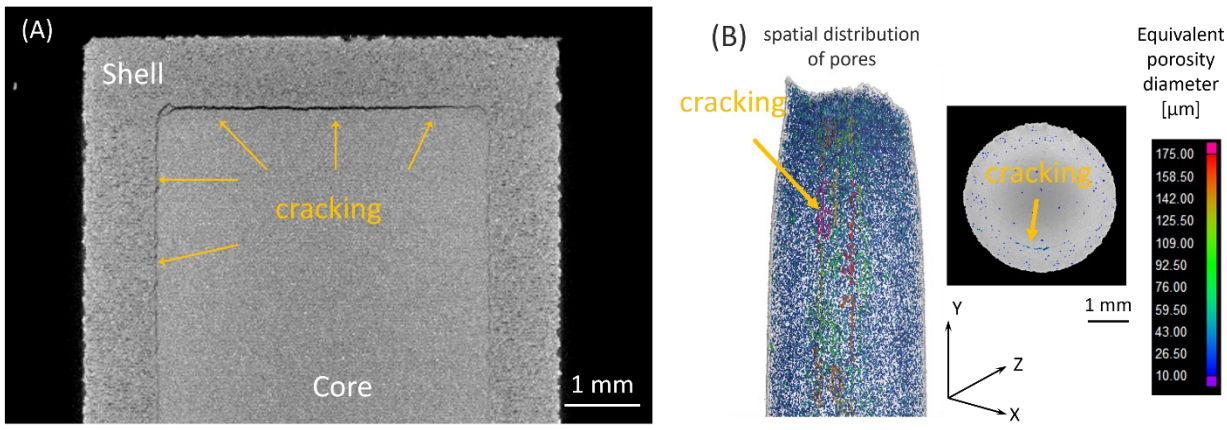

Figure 11. (A) 2D projected µ-CT micrographs from a green sample showing possible cracking at the interface between the top overhang shell structure and its beneath unbound powder. (B) µ-CT showing spatial distribution of pores within the fractured part post-tensile testing, and 2D shadow projections on the XY plane demonstrating the distribution and dimensions of pores as well as appearance of longitudinal cracks.

4. Conclusions

In conclusion, this study investigated the intricate realm of binder jetting additive manufacturing, a revolutionary technique transforming material production and geometric intricacies. The investigation revolved around the interplay between binders and sintering atmospheres in influencing densification behaviors and resultant mechanical properties. A novel binder deposition approach termed "shell printing" was proposed, which strategically deposits binder solely in chosen regions, enabling tailored variations in binder content within green parts. This innovation effectively consolidated unbound powders within a shell geometry. Sintering experiments were performed under two distinct conditions, vacuum and H_2, to unravel the enhancement of densification of both shell and core regions. The research not only unveiled that the green density of bulk specimens was eclipsed by that of shell printed counterparts, but also delved into the intricacies of porosity, grain size, tensile strength, ductility, and fractography. The outcome illustrated the profound impact of shell structure and sintering atmospheres on final microstructure and mechanical attributes of binder jetted components. Specifically, H_2-sintered specimens exhibited reduced density relative to vacuum-sintered counterparts. Grain size analyses pointed to smaller grains in H_2-sintered parts, a consequence of residual pores hindering grain growth. Furthermore, H_2-sintered samples showcased an elongation of 25% and UTS of 460 MPa, while vacuum-sintered parts displayed 70% elongation and UTS of 550 MPa. Fractography analyses using microscopy and µ-CT unveiled ductile fractures in vacuum-sintered samples, whereas H_2-sintered components exhibited a composite fracture mode, encompassing both brittle and ductile features, owing to the presence of residual pores in the microstructure. In essence, this study not only enriches our understanding of the intricate interplay between binder jetting, sintering atmospheres, and resultant material properties but also introduces innovative strategies

that have the potential to transform the perspective of advanced manufacturing, specifically in reactive materials such as copper, titanium, bronze, Ni-Mn based magnetic shape memory alloys, and NiTi shape memory alloys.

Acknowledgments

AM acknowledges the startup funding from the Department of Mechanical, Materials and Aerospace Engineering and Armour College of Engineering at Illinois Institute of Technology in Chicago, Illinois. Authors gratefully acknowledge the Armour R&D undergraduate program from the Dean's Office at Illinois Institute of Technology for particle summer support for EJ, and partial funding from the National Science Foundation [NSF grant number DMR-2050916 and CMMI-2339857]. Authors acknowledge Mohammadreza Asherloo for his assistance with microscopy observations.

References

[1] A. Mostafaei, A.M. Elliott, J.E. Barnes, C.L. Cramer, P. Nandwana, M. Chmielus, Binder jet 3D printing - process parameters, materials, properties, modeling, and challenges, Prog. Mater. Sci. 119 (2021) 100707.

[2] H. Miyanaji, S. Zhang, L. Yang, A new physics-based model for equilibrium saturation determination in binder jetting additive manufacturing process, Int. J. Mach. Tools Manuf. 124 (2018) 1–11.

[3] B. Derby, Inkjet Printing of Functional and Structural Materials: Fluid Property Requirements, Feature Stability, and Resolution, Annu. Rev. Mater. Res. 40 (2010) 395–414.

[4] M. Salehi, S. Maleksaeedi, S.M.L. Nai, G.K. Meenashisundaram, M.H. Goh, M. Gupta, A paradigm shift towards compositionally zero-sum binderless 3D printing of magnesium alloys via capillary-mediated bridging, Acta Mater. 165 (2019) 294–306.

[5] A. Mostafaei, P.R. De Vecchis, M.J. Buckenmeyer, S.R. Wasule, B.N. Brown, M. Chmielus, Microstructural evolution and resulting properties of differently sintered and heat-treated binder jet 3D printed Stellite 6, Mater. Sci. Eng. C. 102 (2019) 276–288.

[6] M. Jamalkhani, M. Asherloo, O. Gurlekce, I.-T. Ho, M. Heim, D. Nelson, A. Mostafaei, Deciphering microstructure-defect-property relationships of vacuum-sintered binder jetted fine 316L austenitic stainless steel powder, Addit. Manuf. 59 (2022) 103133.

[7] M. Castilho, B. Gouveia, I. Pires, J. Rodrigues, M. Pereira, The role of shell/core saturation level on the accuracy and mechanical characteristics of porous calcium phosphate models produced by 3Dprinting, Rapid Prototyp. J. 21 (2015) 43–55.

[8] G. Miao, M. Moghadasi, M. Li, Z. Pei, C. Ma, Binder Jetting Additive Manufacturing: Powder Packing in Shell Printing, J. Manuf. Mater. Process. 7 (2023).

[9] K.M. Rahman, A. Wei, H. Miyanaji, C.B. Williams, Impact of Binder on Part Densification: Enhancing Binder Jetting Part Properties through the Fabrication of Shelled Geometries, Sensors Actuators B. Chem. 62 (2023) 103377.

[10] N. Lecis, M. Mariani, R. Beltrami, L. Emanuelli, R. Casati, M. Vedani, A. Molinari, Effects of process parameters, debinding and sintering on the microstructure of 316L stainless steel produced by binder jetting, Mater. Sci. Eng. A. 828 (2021) 142108.

[11] L. Liu, N. Loh, B. Tay, Constitutive modelling of sintering of 316L stainless steel microsize structures, Appl. Mech. Mater. 149 (2012) 846–851.

[12] J. Li, C. Yuan, J. Guo, J. Hou, L. Zhou, Effect of hot isostatic pressing on microstructure of cast gas-turbine vanes of K452 alloy, Prog. Nat. Sci. Mater. Int. 24 (2014) 631–636.

[13] B. Dzepina, D. Balint, D. Dini, A phase fi eld model of pressure-assisted sintering, J. Eur. Ceram. Soc. 39 (2019) 173–182.

[14] S.L. Taylor, R.N. Shah, D.C. Dunand, Ni-Mn-Ga micro-trusses via sintering of 3D-printed inks containing elemental powders, Elsevier B.V., 2018.

[15] A. Mostafaei, C. Hilla, E.L.E. Stevens, P. Nandwana, A.M. Elliott, M. Chmielus, Comparison of characterization methods for differently atomized nickel-based alloy 625 powders, Powder Technol. 333 (2018) 180–192.

[16] S. Mirzababaei, B.K. Paul, S. Pasebani, Microstructure-property relationship in binder jet produced and vacuum sintered 316 L, Addit. Manuf. 53 (2022) 102720.

[17] T. Do, P. Kwon, C.S. Shin, Process development toward full-density stainless steel parts with binder jetting printing, Int. J. Mach. Tools Manuf. 121 (2017) 50–60.

[18] S.W. Kennedy, Vacuum furnace techniques for metal injection moulded part debinding and sintering, Met. Powder Rep. 45 (1990) 597–599.

[19] G. Shibo, Q. Xuanhui, H. Xinbo, Z. Ting, D. Bohua, Powder injection molding of Ti-6Al-4V alloy, J. Mater. Process. Technol. 173 (2006) 310–314.

[20] R. Frykholm, Y. Takeda, B.-G. Andersson, R. Carlstrom, Solid State Sintered 3-D Printing Component by Using Inkjet (Binder) Method, J. Japan Soc. Powder Powder Metall. 63 (2016) 421–426.

[21] N.D. Parab, J.E. Barnes, C. Zhao, R.W. Cunningham, A.D. Rollett, T. Sun, Real time observation of binder jetting printing process using high-speed X-ray imaging, Sci. Rep. (2019) 28–30.

[22] https://www.additivemonitoring.com/, (n.d.).

[23] N.M. O'Dowd, A.J. Wachtor, M.D. Todd, Effects of digital fringe projection operational parameters on detecting powder bed defects in additive manufacturing, Addit. Manuf. 48 (2021) 102454.

[24] ASTM D790, Standard Test Methods for Flexural Properties of Unreinforced and Reinforced Plastics and Electrical Insulating Materials, 2017.

[25] A. Cabo Rios, T. Mishurova, L. Cordova, M. Persson, G. Bruno, E. Olevsky, E. Hryha, Ex-situ characterization and simulation of density fluctuations evolution during sintering of binder jetted 316L, Mater. Des. 238 (2024) 112690.

[26] A. Mostafaei, E.L. Stevens, E.T. Hughes, S.D. Biery, C. Hilla, M. Chmielus, Powder bed binder jet printed alloy 625: Densification, microstructure and mechanical properties, Mater. Des. 108 (2016) 126–135.

[27] C. Zheng, A. Mostafaei, P.R. de Vecchis, I. Nettleship, M. Chmielus, Microstructure evolution for isothermal sintering of binder jet 3D printed alloy 625 above and below the solidus temperature, Addit. Manuf. 47 (2021) 102276.

[28] A. Mostafaei, Powder bed binder jet 3D printing of Alloy 625: Microstructural evolution,

densification kinetics and mechanical properties (thesis), University of Pittsburgh, 2018.

[29] S.K. Manchili, F. Liu, E. Hryha, L. Nyborg, Carbon-coated iron nanopowder as a sintering aid for water-atomized iron powder, Sci. Rep. 12 (2022) 1–10.

[30] G.A. López, E.J. Mittemeijer, The solubility of C in solid Cu, Scr. Mater. 51 (2004) 1–5.

[31] A.C. Rios, E. Hryha, E. Olesvsky, P. Harlin, Sintering anisotropy of binder jetted 316L stainless steel: part II – microstructure evolution during sintering, Powder Metall. 65 (2022) 283–295.

[32] A. Dudek, R. Włodarczyk, Effect of sintering atmosphere on properties of porous stainless steel for biomedical applications, Mater. Sci. Eng. C. 33 (2013) 434–439.

[33] P. Kumar, R. Jayaraj, J. Suryawanshi, U.R. Satwik, J. McKinnell, U. Ramamurty, Fatigue strength of additively manufactured 316L austenitic stainless steel, Acta Mater. 199 (2020) 225–239.

[34] D. Mati, A. Takasaki, S. Uematsu, Hydrogen Susceptibility of Pre-strained Type 316L Austenitic Stainless Steels in Aqueous Solutions, IOP Conf. Ser. Mater. Sci. Eng. 229 (2017) 0–6.

[35] E. Herms, J.M. Olive, M. Puiggali, Hydrogen embrittlement of 316L type stainless steel, Mater. Sci. Eng. A. 272 (1999) 279–283.

[36] M. Nastac, R.L.A. Klein, Microstructure and mechanical properties comparison of 316L parts produced by different additive manufacturing processes, Solid Free. Fabr. 2017 Proc. 28th Annu. Int. Solid Free. Fabr. Symp. - An Addit. Manuf. Conf. SFF 2017. (2020) 332–341.

[37] A276/A276M-17 Standard Specification for Stainless Steel Bars and Shapes, ASTM International, 2017.

[38] A. Zwiren, Comparison of Binder Jetting Additive Manufacturing to Press and Sinter 316L Stainless Steel, (2018) Corpus ID: 150368018.

[39] N. Kurgan, Effect of porosity and density on the mechanical and microstructural properties of sintered 316L stainless steel implant materials, J. Mater. 55 (2014) 235–241.

[40] P. V. Muterlle, M. Zendron, M. Perina, A. Molinari, Influence of delta ferrite on mechanical properties of stainless steel produced by MIM, 20th Int. Congr. Mech. Eng. (2009) 1–6.

[41] T. Ronneberg, C.M. Davies, P.A. Hooper, Revealing relationships between porosity , microstructure and mechanical properties of laser powder bed fusion 316L stainless steel through heat treatment, Mater. Des. 189 (2020) 108481.

[42] R. Santamaria, M. Salasi, S. Bakhtiari, G. Leadbeater, M. Iannuzzi, Z. Quadir, Microstructure and mechanical behaviour of 316L stainless steel produced using sinter-based extrusion additive manufacturing, J. Mater. Sci. 57 (2021) 9646–9662.

[43] P. Kumar, J. Radhakrishnan, S.S. Gan, A. Bryl, J. McKinnell, U. Ramamurty, Tensile and fatigue properties of the binder jet printed and hot isostatically pressed 316L austenitic stainless steel, Mater. Sci. Eng. A. 868 (2023) 144766.

[44] B. Verlee, T. Dormal, J. Lecomte-Beckers, Density and porosity control of sintered 316L stainless steel parts produced by additive manufacturing, Powder Metall. 55 (2012) 260–267.

[45] J. Damon, S. Dietrich, S. Gorantla, U. Popp, B. Okolo, V. Schulze, Process porosity and mechanical performance of fused filament fabricated 316L stainless steel, Rapid Prototyp. J. 25 (2019) 1319–1327.

[46] ASTM A666-15; Standard Specification for Annealed or Cold-Worked Austenitic Stainless Steel Sheet, Strip, Plate, and Flat Bar; ASTM International: West Conshonhocken, PA, USA, in: 2014.

[47] J. Cai, B. Zhang, X. Qu, Microstructure evolution and mechanical behavior of SS316L alloy

fabricated by a non-toxic and low residue binder jetting process, Appl. Surf. Sci. 616 (2023) 156589.

[48] P. Kumar, R. Jayaraj, S.S. Gan, A. Bryl, J. McKinnell, U. Ramamurty, Tensile and fatigue properties of the binder jet printed and hot isostatically pressed 316L austenitic stainless steel, Mater. Sci. Eng. A. (2022) 144766.